# Color-octet quarkonia production

Peter Cho and Adam K. Leibovich
*Lauritsen Laboratory, California Institute of Technology, Pasadena, California 91125*
(Received 25 May 1995)

Gluon fragmentation represents the dominant source of high energy prompt quarkonia at hadron colliders. Fragmentation approximations break down, however, when a quarkonium's transverse momentum becomes comparable to its mass. In this paper we identify a large class of color-octet diagrams that mediate quarkonia production at all energies and reduce to the dominant set of gluon fragmentation graphs in the high $p_\perp$ limit. They contribute to quarkonia differential cross sections at the same order as color-singlet diagrams and bring theoretical predictions for $\Upsilon$ and $\Psi$ production at the Fermilab Tevatron into agreement with experimental measurements. Using recent CDF data we extract numerical values for bottomonia and charmonia color-octet matrix elements which are consistent with NRQCD scaling rules. We also find that quarkonia generated via the color-octet mechanism are strongly polarized at low as well as high energies. Spin alignment measurements can thus test the color-octet quarkonia production picture.

PACS number(s): 14.40.Gx, 13.87.Fh

## I. INTRODUCTION

The theory of quarkonia production has recently undergone a number of significant developments. Progress in this area was stimulated by the discovery of Braaten and Yuan in 1993 that parton fragmentation represents the dominant source of prompt quarkonia at high energies [1]. These authors realized that the fragmentation functions which specify the probability for gluons and heavy quarks to hadronize into quarkonia bound states can be calculated starting from first principles in QCD. Over the past few years, the most important fragmentation functions for $S$- and $P$-wave quarkonia have been computed to lowest order [1–5]. They have subsequently been utilized to investigate a range of issues related to quarkonium phenomenology.

One of the most interesting applications of this fragmentation work has been to the study of prompt charmonium production at the Fermilab Tevatron [6–8]. Comparison between theoretical predictions and experimental measurements of $J/\psi$ and $\psi'$ differential cross sections clearly demonstrate that fragmentation dominates over all other charmonium creation mechanisms at large transverse momenta. Orders of magnitude discrepancies between cross-section computations and observations are significantly reduced when gluon and charm fragmentation processes are taken into account. The predicted prompt $J/\psi$ rate then qualitatively agrees with recent data from the Collider Detector at Fermilab (CDF) Collaboration [9,10]. In the case of $\psi'$ production, the fragmentation results substantially improve upon earlier differential cross section predictions. But they still underestimate the number of $\psi'$'s observed at the Tevatron by approximately a factor of 50. This large discrepancy between theory and experiment indicates that some important production mechanism beyond the simplest $g \to \psi'$ and $c \to \psi'$ fragmentation processes needs to be included. A number of possible resolutions to the $\psi'$ problem have been suggested [11–14], and experimental studies which may confirm or reject these proposals are underway.

Although the fragmentation picture of quarkonium production has provided valuable insight, its validity domain is restricted to high energies. The approximations that enter into fragmentation function computations break down when a quarkonium's energy becomes comparable to its mass. Fragmentation predictions for charmonium differential cross sections are therefore unreliable at low transverse momenta. Similarly, fragmentation results for bottomonium production are untrustworthy throughout the $p_\perp < 15$ GeV region where Tevatron data exist. Yet even in this low energy regime, $\Upsilon$ cross section measurements significantly disagree with existing theoretical predictions [10,15].

The discrepancies in the $\Upsilon$ sector provide the primary motivation for the work which we present in this paper. Building upon several recently developed ideas in heavy quarkonium physics, we identify a large class of color-octet diagrams that mediate quarkonia production at all energies and reduce to the dominant set of gluon fragmentation graphs in the high $p_\perp$ limit. These diagrams enter at the same order into prompt production processes as previously considered color-singlet graphs and must be included for consistency. As we shall see, the addition of color-octet contributions to $\Upsilon$ production computations significantly improves agreement between theory and experiment.

Our article is organized as follows. In Sec. II, we discuss the short- and long-distance factorization of quarkonia production amplitudes. We then calculate the leading color-octet contributions to quarkonia differential cross sections. In Sec. III we apply the color-octet cross sections to the study of $\Upsilon$ and $\Psi$ production at the Tevatron. Using CDF data we extract numerical values for bottomonia and charmonia color-octet matrix elements which we compare with nonrelativistic QCD scaling relations in Sec. IV. We next analyze the spin alignment of

 

quarkonia generated via the color-octet mechanism as a function of transverse momentum in Sec. V. Finally, we summarize our findings in Sec. VI and close with some thoughts on directions for future work.

## II. COLOR-OCTET CONTRIBUTIONS TO QUARKONIA CROSS SECTIONS

The physics of quarkonia involves several different energy scales that are separated by the small velocity $v$ of the two heavy constituents inside $Q\bar{Q}$ bound states [16]. The first is set by the quark mass $M_Q$ which fixes the distance range for $Q\bar{Q}$ creation and annihilation processes. The second is given by the heavy constituents' typical momentum $M_Q v$ which is inversely proportional to the bound state's spatial size. The kinetic energy $M_Q v^2$ represents a third important quarkonium energy scale and determines the constituents' characteristic interaction time. As $M_Q \to \infty$, the heavy constituents' velocity $v \sim 1/\ln M_Q$ tends towards zero, and these three scales become widely separated:

$$(M_Q v^2)^2 \ll (M_Q v)^2 \ll M_Q^2 \; . \tag{2.1}$$

This hierarchy is well realized in the real world for bottomonia with $v_b^2 \simeq 0.08$ and to a lesser extent for charmonia with $v_c^2 \simeq 0.23$.

The presence of these different distance scales renders the study of quarkonia both interesting and challenging. An effective field theory formalism called nonrelativistic quantum chromodyanmics (NRQCD) has been established to systematically keep track of this scale hierarchy [16,17]. It is based upon a double power series expansion in the strong interaction fine structure constant $\alpha_s = g_s^2/4\pi$ and the small velocity parameter $v$. Short-distance processes which occur at energies comparable to or greater than the heavy quark mass are perturbatively computable within the effective theory. Long-distance effects are consolidated into nonperturbative matrix elements whose values must be determined from experiment or the lattice. High and low energy interactions are thus cleanly separated in NRQCD, and simple power counting rules methodically determine the dominant contributions to various quarkonium processes [18]. We will work within the NRQCD framework throughout this paper.

Before the development of NRQCD, quarkonia were generally treated as nonrelativistic bound states of a heavy quark and antiquark in a static gluon field that sets up an instantaneous confining potential [19]. Although this picture has enjoyed a remarkable degree of phenomenological success, it fails to take into account gluons inside a quarkonium with wavelengths much greater than the bound state's naive size. The presence of such low energy gluons implies that the heavy quark and antiquark cannot always be regarded as residing in a color-singlet configuration.

This shortcoming of the potential model approach is rectified in NRQCD. Dynamical gluons enter into Fock state decompositions of physical quarkonium states. For example, wave functions of $S$-wave orthoquarkonia schematically appear in Coulomb gauge as

$$\begin{aligned}|\psi_Q\rangle = {} & O(1)|Q\bar{Q}[^3S_1^{(1)}]\rangle + O(v)|Q\bar{Q}[^3P_J^{(8)}]g\rangle \\ & + O(v^2)|Q\bar{Q}[^3S_1^{(1,8)}]gg\rangle + O(v^2)|Q\bar{Q}[^1S_0^{(8)}]g\rangle + O(v^2)|Q\bar{Q}[^3D_J^{(1,8)}]gg\rangle + \cdots \; .\end{aligned} \tag{2.2}$$

The angular momentum quantum numbers of the $Q\bar{Q}$ pairs within the various Fock components are indicated in spectroscopic notation inside the square brackets, and their color configurations are labeled by singlet or octet superscripts. $S$-wave quarkonia reactions proceed at lowest order in the velocity expansion through the first Fock state in (2.2). The $Q\bar{Q}$ pair in this $O(1)$ Fock component has precisely the same angular momentum and color quantum numbers as the full quarkonium state. The NRQCD description of $\psi_Q$ production or annihilation thus reduces to the familiar color-singlet model in the $v \to 0$ limit.

$P$-wave orthoquarkonia processes are more complicated. They are mediated at leading order in the velocity expansion by the first two Fock states in the $\chi_{QJ}$ wave function

$$|\chi_{QJ}\rangle = O(1)|Q\bar{Q}[^3P_J^{(1)}]\rangle + O(v)|Q\bar{Q}[^3S_1^{(8)}]g\rangle + \cdots \; . \tag{2.3}$$

Contributions to $\chi_{QJ}$ formation which involve the first color-singlet Fock component are proportional to the squared derivative of the $P$-wave bound state's wave function at the origin. This quantity counts as $O(v^5)$ in the NRQCD velocity expansion. On the other hand, creation of the $S$-wave color-octet $Q\bar{Q}$ pair in the second Fock state of (2.3) takes place at $O(v^3)$. The subsequent evolution of the $Q\bar{Q}[^3S_1^{(8)}]$ pair into a colorless $\chi_{QJ}$ hadron via the emission or absorption of a soft gluon costs an additional power of $v$ in the amplitude and $v^2$ in the rate. So $\chi_{QJ}$ production proceeds at $O(v^5)$ in both the color-singlet and color-octet channels [4].

It is useful to draw a picture which clarifies the difference between these two quarkonium production mechanisms. In Fig. 1(a), we illustrate a typical color-singlet Feynman graph that creates a $\chi_{QJ}$. The $O(\alpha_s^3)$ hard scattering forms a colorless $Q\bar{Q}[^3P_J^{(1)}]$ pair at a short-distance scale. The heavy quark and antiquark fly out from the initial collision point in nearly parallel directions and almost on mass shell. After exchanging many soft gluons, the color-singlet $Q\bar{Q}$ pair eventually hadronizes at a long distance into a $\chi_{QJ}$ bound state. In Fig. 1(b), the $O(\alpha_s^3)$ high energy collision creates a $Q\bar{Q}$ pair in a color-octet configuration. Far away from the collision point, the $Q\bar{Q}[^3S_1^{(8)}]$ pair emits a long wavelength gluon which bleeds off its color but carries away virtually no energy or momentum. The heavy pair thus transforms

into a colorless $\chi_{QJ}$ quarkonium state.

Color-singlet quarkonium production has been studied for years. Leading order color-singlet differential cross sections were calculated a decade ago [20–22], and some total cross section formulas have been evaluated at next-to-leading order as well [23]. In contrast, color-octet contributions to quarkonium processes have only recently begun to be considered. While the latter mechanism may be less familiar than the former, it is certainly not less important. As can be seen in Fig. 1, color-singlet and color-octet graphs arise at the same order in $\alpha_s$. Moreover, the color-octet diagrams dominate at high energies. So a complete analysis of quarkonium production at hadron colliders must include both mechanisms.

Color-octet creation of $S$-wave orthoquarkonia starts at $O(\alpha_s^2)$ via the $q\bar{q} \to \psi_Q$ Feynman diagram shown in Fig. 2. As indicated by the dashed line in the figure, the total color-octet amplitude factorizes into short- and long-distance pieces:

$$\mathcal{A}(q\bar{q} \to \psi_Q(nS))_{\text{octet}} = \mathcal{A}(q\bar{q} \to Q\bar{Q}[^3S_1^{(8)}])_{\text{short distance}} \times \mathcal{A}(Q\bar{Q}[^3S_1^{(8)}] \to \psi_Q(nS))_{\text{long distance}} . \tag{2.4}$$

The short-distance part of the quark-antiquark fusion process lies to the left of the dashed line in Fig. 2 and can be calculated within perturbative QCD. On the other hand, the long-distance component to the right of the dashed line involves nonperturbative physics. We will consider these two factors in turn.

To begin, we examine the subamplitude for virtual gluon formation of a color-octet $Q\bar{Q}$ pair

$$\mathcal{A}(g_a^* \to Q\bar{Q}[^3S_1^{(8)}]_b)_\mu = \sum_{s_1,s_2} \sum_{i,j} \bar{u}\left(\frac{P}{2} + q; s_1\right) g_s \gamma_\mu (T_a)^i_j v\left(\frac{P}{2} - q; s_2\right) \langle \tfrac{1}{2} s_2; \tfrac{1}{2} s_2 | 1 S_z \rangle \langle 3i; \bar{3}j | 8b \rangle , \tag{2.5}$$

which is illustrated in Fig. 3. The heavy quark and antiquark propagate nearly on-shell with a large combined momentum $P$ and a small relative momentum $q$. The spin and color quantum numbers for the $Q\bar{Q}$ pair are projected out by the sums over the SU(2) and SU(3) Clebsch-Gordan coefficients $\langle \frac{1}{2} s_1; \frac{1}{2} s_2 | 1 S_z \rangle$ and $\langle 3i; \bar{3}j | 8b \rangle = \sqrt{2}(T_b)^j_i$. The subamplitude may be rewritten in the trace form

$$\mathcal{A}(g_a^* \to Q\bar{Q}[^3S_1^{(8)}]_b)_\mu = \sqrt{2} g_s \mathrm{Tr}(T_a T_b) \mathrm{Tr}[\gamma_\mu P_{1Sz}(P; q)] , \tag{2.6}$$

where

$$P_{SSz}(P; q) = \sum_{s_1,s_2} v\left(\frac{P}{2} - q; s_2\right) \bar{u}\left(\frac{P}{2} + q; s_1\right) \langle \tfrac{1}{2} s_1; \tfrac{1}{2} s_2 | S S_z \rangle \tag{2.7}$$

denotes a spin projection operator.[1] This $4 \times 4$ matrix reduces to the covariant expressions

$$\begin{aligned} P_{00}(P; q) &= \frac{-1}{2\sqrt{2} M_Q} \left(\frac{\not{P}}{2} - \not{q} - M_Q\right) \gamma^5 \left(\frac{\not{P}}{2} + \not{q} + M_Q\right) , \\ P_{1Sz}(P; q) &= \frac{-1}{2\sqrt{2} M_Q} \left(\frac{\not{P}}{2} - \not{q} - M_Q\right) \not{\epsilon}^*(P; S_z) \left(\frac{\not{P}}{2} + \not{q} + M_Q\right) , \end{aligned} \tag{2.8}$$

up to $O(q^2)$ corrections. The projection operators' dependence on $q$ is irrelevant for $S$-wave $Q\bar{Q}$ production. The $g^* \to Q\bar{Q}[^3S_1^{(8)}]$ subamplitude consequently simplifies to

$$\mathcal{A}(g_a^* \to Q\bar{Q}[^3S_1^{(8)}]_b)_\mu = g_s M \epsilon^*_\mu(P; S_z) \delta_{ab} , \tag{2.9}$$

where $M = 2M_Q$ denotes the mass of the heavy quark-antiquark pair. Combining this result with the remaining perturbative part of the Feynman graph in Fig. 2, we determine the short-distance matrix element in Eq. (2.4):

$$\mathcal{A}(q(p_1)\bar{q}(p_2) \to Q\bar{Q}[^3S_1^{(8)}]_a)_{\text{short distance}} = \frac{g_s^2}{M} \bar{v}(p_2) \gamma^\mu T_a u(p_1) \epsilon^*_\mu(p_1 + p_2; S_z) . \tag{2.10}$$

Once the color-octet $Q\bar{Q}$ pair has been formed, it can evolve into a physical $\psi_Q$ bound state in many different ways. For example, it may absorb a soft gluon and transform into a $\chi_{QJ}$ through the second Fock component in (2.3) at

[1] Spin projection matrices were originally introduced in Refs. [24,25]. The $\bar{u}$ and $v$ spinors in our definition of $P_{SSz}$ correspond to an outgoing $Q\bar{Q}$ pair. They differ from the $\bar{v}$ and $u$ spinors appearing in these earlier articles' spin projection operators. Our $(+,-,-,-)$ metric signature convention is also opposite to that of Ref. [25].

$O(v^5)$ in the velocity expansion. The $P$-wave quarkonium can subsequently emit a photon and decay to the $S$-wave state. Alternatively at $O(v^7)$, the color-octet $Q\bar{Q}$ pair may emit two long wavelength gluons in a double chromoelectric dipole transition and turn into a color-singlet $Q\bar{Q}$ pair that has order unity overlap with the full $\psi_Q$ wave function in (2.2). All possible ways to produce a $\psi_Q$ starting from a $Q\bar{Q}[^3S_1^{(8)}]$ pair are encoded into the long-distance amplitude in Eq. (2.4). This factor is pictorially represented by the big blob in Fig. 2 with the long wavelength gluon tail. It cannot be computed from first principles without resorting to lattice QCD. But since the low energy dependence of interactions that take place inside the blob is negligible, the nonperturbative amplitude is simply a constant:

$$\mathcal{A}(Q\bar{Q}[^3S_1^{(8)}] \to \psi_Q(nS))_{\text{long distance}} = \text{const.} \tag{2.11}$$

The total $Q\bar{Q}[^3S_1^{(8)}]$ contribution to $\psi_Q$ production thus involves one free parameter which we will eventually have to fit.

We turn now to investigate the gluon fusion process $gg \to \psi_Q$. The color-octet amplitude for this reaction which proceeds through an intermediate $Q\bar{Q}[^3S_1^{(8)}]$ state again factorizes into short- and long-distance pieces:

$$\mathcal{A}(gg \to \psi_Q(ns))_{\text{octet}} = \mathcal{A}(gg \to Q\bar{Q}[^3S_1^{(8)}])_{\text{short distance}} \times \mathcal{A}(Q\bar{Q}[^3S_1^{(8)}] \to \psi_Q(nS))_{\text{long distance}} . \tag{2.12}$$

The long-distance term is precisely the same as in Eq. (2.11). The short-distance factor involves at lowest order the three Feynman diagrams displayed in Fig. 4. Evaluating the high energy gluonic matrix element in a similar fashion to its quark counterpart in (2.10), we deduce

$$\begin{aligned}\mathcal{A}(g_a(p_1)g_b(p_2) \to Q\bar{Q}[^3S_1^{(8)}]_c)_{\text{short distance}} = {} & \frac{ig_s^2}{M} f_{abc}\varepsilon^\mu(p_1)\varepsilon^\nu(p_2)\varepsilon^\sigma(p_1+p_2;S_z)^* \\ & \times \frac{p_1^2+p_2^2}{p_1^2+p_2^2-M^2}[(p_2-p_1)_\sigma g_{\mu\nu} + 2(p_{1\nu}g_{\mu\sigma} - p_{2\mu}g_{\nu\sigma})] .\end{aligned} \tag{2.13}$$

It is important to observe that this expression vanishes when both incoming gluons are on-shell. This result is consistent with Yang's theorem which forbids a massive $J = 1$ vector boson from decaying to two massless $J = 1$ bosons [26]. In fact, the theorem requires that the on-shell $gg \to Q\bar{Q}[^3S_1^{(8)}]$ amplitude vanish to all orders. The color-octet diagrams in Fig. 4 consequently participate in quarkonium production only as subgraphs inside more complicated reactions.

Color-octet pairs with orbital angular momentum and spin quantum numbers different than $L = 0$ and $S = 1$ also mediate $gg \to \psi_Q$ fusion at $O(\alpha_s^2)$. In particular, $Q\bar{Q}[^3P_J^{(8)}]$ and $Q\bar{Q}[^1S_0^{(8)}]$ which have opposite charge conjugation properties relative to $Q\bar{Q}[^3S_1^{(8)}]$ can be produced via the first and second diagrams in Fig. 4. Although the former intermediate states are generated at the same order in the $\alpha_s$ expansion as the latter, they participate in $\psi_Q$ production starting at $O(v^7)$ which is formally subleading in the velocity expansion. For simplicity, we will neglect all effects from colored heavy pairs other than $Q\bar{Q}[^3S_1^{(8)}]$ in our present analysis. We will return to study the potentially important contributions to quarkonia production from $Q\bar{Q}[^3P_J^{(8)}]$ and $Q\bar{Q}[^1S_0^{(8)}]$ intermediate states in a future publication [27].

$O(\alpha_s^2)$ scattering processes create quarkonia at small transverse momenta that differ from zero only as a result of the incident partons' intrinsic hadronic motion. Since outgoing states from $2 \to 1$ collisions are lost down the beampipe, we need to consider $2 \to 2$ transitions which produce quarkonia with experimentally measurable $p_\perp$. Such reactions start at $O(\alpha_s^3)$ and proceed in both the color-singlet and color-octet mechanisms through the partonic channels $q\bar{q} \to Q\bar{Q}[^{2S+1}L_J^{(C)}]g$,

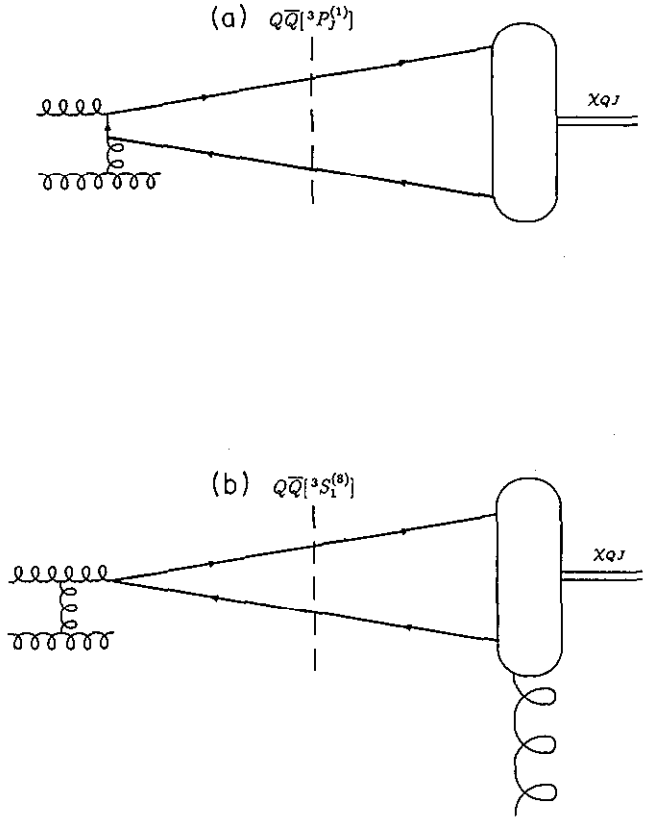


FIG. 1. Typical Feynman graphs which contribute to $\chi_{QJ}$ production at $O(\alpha_s^3)$ through the (a) color-singlet and (b) color-octet mechanisms. The short-distance scattering collisions, respectively, create $Q\bar{Q}$ pairs in $^3P_J^{(1)}$ and $^3S_1^{(8)}$ configurations. The $Q\bar{Q}$ pairs hadronize at long distances into $\chi_{QJ}$ bound states.

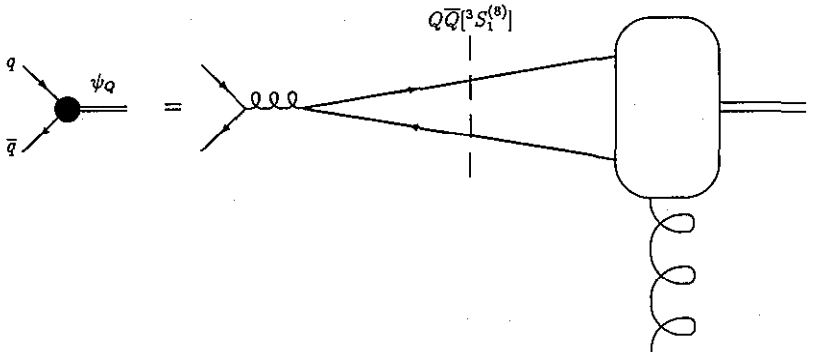


FIG. 2. Color-octet diagram which mediates $q\bar{q} \to \psi_Q$ production at $O(\alpha_s^2)$.

$gq \to Q\bar{Q}[^{2S+1}L_J^{(C)}]q$ and $gg \to Q\bar{Q}[^{2S+1}L_J^{(C)}]g$. The differential cross sections for the color-singlet modes were calculated in Refs. [20–22]. We present their color-octet analogues below.

The Feynman diagrams which generate $\psi_Q$ quarkonia in the three different partonic modes through the color-octet mechanism are illustrated in Figs. 5(a)–5(c). The shaded circles in these figures represent the $q\bar{q} \to \psi_Q$ and $gg \to \psi_Q$ amplitudes in Eqs. (2.4) and (2.12). The sums of the graphs in each channel yield gauge invariant amplitudes. Their spin and color averaged squares are given by

$$\overline{\sum}|\mathcal{A}(q\bar{q} \to \psi_Q g)|^2 = \frac{512\pi^3\alpha_s^3}{27M^2}\frac{\hat{t}^2+\hat{u}^2+2M^2\hat{s}}{\hat{t}\hat{u}(\hat{s}-M^2)^2}[4(\hat{t}^2+\hat{u}^2)-\hat{t}\hat{u}]\mathcal{M}_8(\psi_Q)\ , \tag{2.14a}$$

$$\overline{\sum}|\mathcal{A}(gq \to \psi_Q q)|^2 = -\frac{64\pi^3\alpha_s^3}{9M^2}\frac{\hat{s}^2+\hat{u}^2+2M^2\hat{t}}{\hat{s}\hat{u}(\hat{t}-M^2)^2}[4(\hat{s}^2+\hat{u}^2)-\hat{s}\hat{u}]\mathcal{M}_8(\psi_Q)\ , \tag{2.14b}$$

$$\overline{\sum}|\mathcal{A}(gg \to \psi_Q g)|^2 = -\frac{32\pi^3\alpha_s^3}{3M^2}\frac{27(\hat{s}\hat{t}+\hat{t}\hat{u}+\hat{u}\hat{s})-19M^4}{[(\hat{s}-M^2)(\hat{t}-M^2)(\hat{u}-M^2)]^2}$$
$$\times[(\hat{t}^2+\hat{t}\hat{u}+\hat{u}^2)^2-M^2(\hat{t}+\hat{u})(2\hat{t}^2+\hat{t}\hat{u}+2\hat{u}^2)+M^4(\hat{t}^2+\hat{t}\hat{u}+\hat{u}^2)]\mathcal{M}_8(\psi_Q)\ , \tag{2.14c}$$

where $\mathcal{M}_8(\psi_Q) \equiv |\mathcal{A}(Q\bar{Q}[^3S_1^{(8)}] \to \psi_Q(nS))|^2$. The squared matrix element in (2.14a) and (2.14b) were determined using standard spinor summation techniques. The result in (2.14c) was obtained from a simple helicity amplitude method which obviated the need to compute a large number of interference terms. We calculated the 24 different helicity amplitudes for $gg \to \psi_Q g$ scattering by choosing explicit representations for the massless and massive vector boson momenta and polarizations in the parton center-of-mass frame.[2] The amplitudes were then individually squared and added together using the high energy physics MATHEMATICA package FEYNCALC [28].

The squared matrix element in Eq. (2.14a) diverges when either of the partonic Mandelstam invariants $\hat{t}$ or

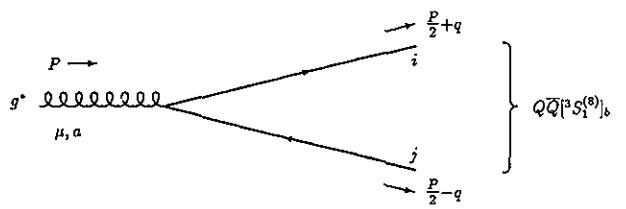


FIG. 3. Lowest order contribution to the $g^* \to Q\bar{Q}[^3S_1^{(8)}]$ subamplitude in Eq. (2.5).

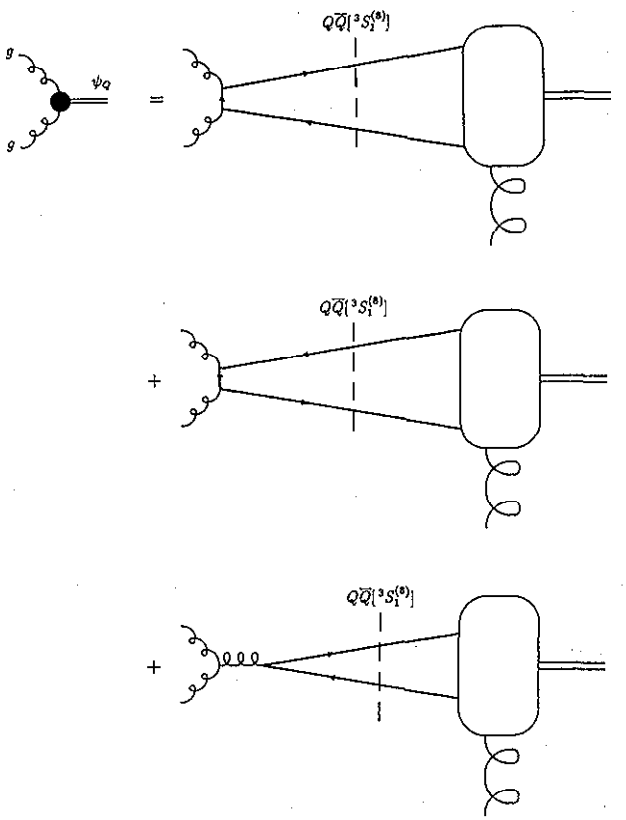


FIG. 4. Color-octet diagrams which mediate $gg \to \psi_Q$ production at $O(\alpha_s^2)$. The sum of these graphs vanishes when both incoming gluons are on-shell.

[2]Parity and crossing symmetry relations imply that only 4 of the 24 $gg \to \psi_Q g$ helicity amplitudes are independent.

$\hat{u}$ approach zero. The source of these long-distance infinities can be identified by looking at Fig. 5(a). As the outgoing gluon in a $q\bar{q} \to \psi_Q g$ collision becomes collinear with either the incoming quark or antiquark, the exchanged fermion in the $t$ or $u$-channel graphs goes on shell and its propagator blows up. The divergence generated by the collinear splitting of the incident parton may be factored into its distribution function. The hard scattering reaction then reduces to the $q\bar{q} \to \psi_Q$ Born level process illustrated in Fig. 2. A similar $u$-channel collinear divergence develops in the squared $gq \to \psi_Q q$ amplitude when the four-momenta of the incoming gluon and outgoing quark become proportional. In contrast, the $t$-channel diagram in Fig. 5(b) remains finite. The pole in the intermediate propagator is canceled by the zero in the $gg \to \psi_Q$ amplitude as the $t$-channel gluon goes on shell. This same cancellation renders $\overline{\sum}|\mathcal{A}(gg \to \psi_Q q)|^2$ free of long-distance infinities.

The squared color-octet amplitudes in (2.14) enter into the partonic differential cross section

$$\frac{d\sigma}{d\hat{t}}(ab \to \psi_Q c)_{\text{octet}} = \frac{1}{16\pi\hat{s}^2}\overline{\sum}|\mathcal{A}(ab \to \psi_Q c)|^2 \ , \quad (2.15)$$

which appears in turn within the triple differential hadronic expression

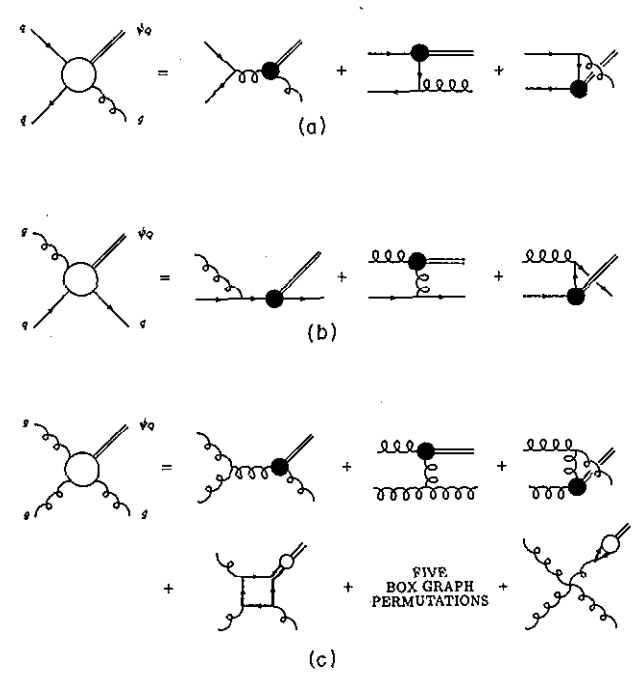


FIG. 5. Color-octet diagrams which mediate (a) $q\bar{q} \to \psi_Q g$, (b) $gq \to \psi_Q q$, and (c) $gg \to \psi_Q g$ scattering at $O(\alpha_s^3)$. The shaded circles appearing in these graphs represent the $q\bar{q} \to \psi_Q$ and $gg \to \psi_Q$ amplitudes pictured in Figs. 2 and 4.

$$\frac{d^3\sigma}{dy_3 dy_4 dp_\perp}(AB \to \psi_Q X)_{\text{octet}} = 2p_\perp \sum_{abc} x_a x_b f_{a/A}(x_a) f_{b/B}(x_b) \frac{d\sigma}{d\hat{t}}(ab \to \psi_Q c)_{\text{octet}} \ . \quad (2.16)$$

The partonic cross section is multiplied by distribution functions $f_{a/A}(x_a)$ and $f_{b/B}(x_b)$ that specify the probability of finding partons $a$ and $b$ inside hadrons $A$ and $B$ carrying momentum fractions $x_a$ and $x_b$. The product is then summed over parton channels. The resulting hadronic cross section is a function of the $\psi_Q$ and recoiling jet rapidities $y_3$ and $y_4$ and their common transverse momentum $p_\perp$.

It is instructive to examine the high energy limit of color-octet quarkonia production. As the partonic Mandelstam invariants grow to infinity, the cross section in Eq. (2.15) reduces to

$$\frac{d\sigma}{d\hat{t}}(ab \to \psi_Q c)_{\text{octet}} \overset{\hat{s}\to\infty}{\to} \frac{d\sigma}{d\hat{t}}(ab \to g^* c) \times \left(\frac{1}{M^2}\right)^2 \times |\mathcal{A}(g^* \to \psi_Q)|^2 \ . \quad (2.17)$$

This asymptotic expression has a simple gluon fragmentation interpretation. The first factor represents the differential cross section for producing a high energy virtual gluon. The second term comes from the square of the gluon's propagator. The last factor equals the square of the amplitude in Eq. (2.9) times $\mathcal{M}_8(\psi_Q)$ and determines the virtual gluon's probability to hadronize into a $\psi_Q$ bound state. The gluon fragmentation picture for heavy quarkonium production is thus precisely recovered in the high energy limit [1].

Gluon fragmentation via the color-octet mechanism represents the dominant source of large $p_\perp$ quarkonia at hadron colliders [4,6,11]. The total cross section for $\psi_Q$ production reduces at high energies to the fragmentation form

$$\frac{d^3\sigma}{dy_3 dy_4 dp_\perp}(AB \to \psi_Q X)_{\text{frag}} = \int_0^1 dz \frac{d^3\sigma}{dy_3 dy_4 dp_\perp}\left[AB \to g\left(\frac{p_\perp}{z}\right)X, \mu\right] D_{g\to\psi_Q}(z,\mu) \ . \quad (2.18)$$

The gluon fragmentation function evaluated at the factorization scale $\mu = M$ is readily identified from Eq. (2.17):

$$D_{g\to\psi_Q}(z,M) = \frac{4\pi\alpha_s(M)\mathcal{M}_8(\psi_Q)}{M^2}\delta(1-z) \ . \quad (2.19)$$

Leading log QCD corrections to this result may be summed by using the Altarelli-Parisi equation

$$\mu\frac{dD_{g\to\psi_Q}}{d\mu}(z,\mu) = \frac{\alpha_s(\mu)}{\pi}\int_z^1 \frac{dy}{y} P_{gg}(y) D_{g\to\psi_Q}\left(\frac{z}{y},\mu\right) \ , \quad (2.20)$$

where

$$P_{gg}(y) = 6\left[\frac{y}{(1-y)_+} + \frac{1-y}{y} + y(1-y) + \frac{33-2n_f}{36}\delta(1-y)\right] \quad (2.21)$$

denotes the gluon splitting function for $n_f$ active quark flavors. At high energies, the fragmentation approximation in (2.18) incorporates sizable $O[\ln(E^2/M^2)]$ renormalization effects, and its intrinsic $O(M^2/E^2)$ errors are negligible. In contrast, the color-octet formula in (2.16) does not include any QCD corrections which are small at low $p_\perp$, but it retains full dependence upon all $O(M^2/E^2)$ terms. These two forms for the $\psi_Q$ differential cross section are thus complementary.

We may exercise our perturbative freedom to supplement the $O(\alpha_s^3)$ color-octet cross section with the leading logarithms from the gluon fragmentation approach. We implement this choice as follows:

$$d\sigma(AB \to \psi_Q X)_{\rm interp} = d\sigma(AB \to \psi_Q X)_{\rm octet} \times \frac{d\sigma(AB \to \psi_Q X)_{\rm frag\ with\ QCD\ running}}{d\sigma(AB \to \psi_Q X)_{\rm frag\ without\ QCD\ running}} . \tag{2.22}$$

The ratio on the right-hand side of this hybrid expression reduces to unity at low energy, whereas the first factor over the denominator approaches unity at high energy. Equation (2.22) therefore smoothly interpolates between the two asymptotic limits in Eqs. (2.16) and (2.18). We will use this final color-octet formula to study bottomonia and charmonia production at the Tevatron in the following section.

## III. $\Upsilon$ AND $\Psi$ PRODUCTION AT THE TEVATRON

The CDF Collaboration has recently measured $\Upsilon$ production at the Tevatron for the first time [15]. Their reported $\Upsilon(1S)$, $\Upsilon(2S)$, and $\Upsilon(3S)$ transverse momentum differential cross sections seriously disagree with predictions based upon $O(\alpha_s^3)$ color-singlet cross section formulas. Some discrepancy between the theoretical and experimental findings may be attributed to various parameter uncertainties and higher order corrections. For example, different quarkonia potential models yield estimates for long-distance color-singlet matrix elements that can disagree by as much as 100% [29]. Similarly, renormalization scale dependence of lowest order hard scattering cross sections introduces a sizable error. Different choices for parton distribution functions also yield slight variations in final results. In short, existing predictions for $\Upsilon$ production can probably only be trusted at the factor of 2 level [6,8,30]. Nonetheless, the magnitude of disparity between old theoretical estimates and new experimental measurements strongly suggests that additional mechanisms beyond the simplest color-singlet processes are at work. As we shall see, inclusion of color-octet reactions brings the predicted cross sections into line with the $\Upsilon$ data.

We first investigate the differential cross section for $\Upsilon(1S)$ production in the rapidity range $|y| \le 0.4$. The color-singlet distribution is illustrated by the dashed curve in Fig. 6.[3] It includes direct $\Upsilon(1S)$ production as well as radiative feeddown from $\chi_{bJ}(1P)$ and $\chi_{bJ}(2P)$ states. Additional contributions from strong and electromagnetic decays of $\Upsilon(2S)$ and $\Upsilon(3S)$ are negligible. In computing the color-singlet cross sections, we adopt the radial wave function values tabulated in Ref. [29] for the Buchmüller-Tye QCD potential [31] and the associated bottom quark mass $M_b = 4.88$ GeV. The color-singlet prediction for $\Upsilon(1S)$ production clearly underestimates the CDF data points shown in the figure.

The dot-dashed curve in Fig. 6 displays the color-octet contribution to the $\Upsilon(1S)$ differential cross section. The best fit value $\mathcal{M}_8(\Upsilon(1S)) = (3.66 \pm 0.27) \times 10^{-3}$ GeV$^2$ for its squared long-distance matrix element determines the probability for a $b\bar{b}[^3S_1^{(8)}]$ pair to hadronize into an $\Upsilon(1S)$. Following Eq. (2.22), we have incorporated leading log QCD corrections into the color-octet cross section. The dot-dashed curve therefore approaches by construc-

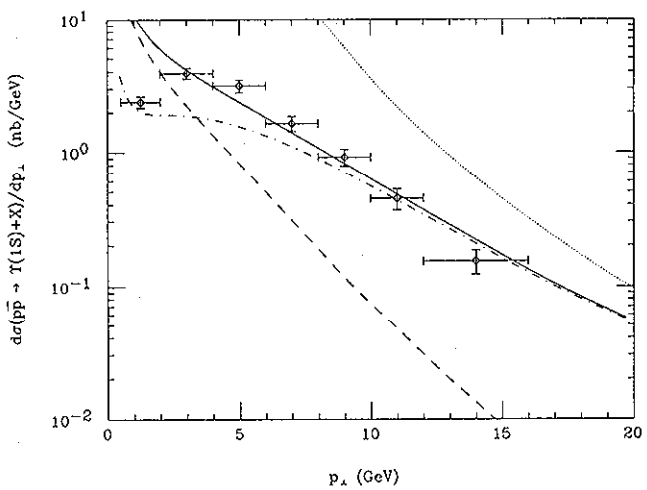


FIG. 6. Theoretical transverse momentum differential cross section for $\Upsilon(1S)$ production at the Tevatron in the rapidity interval $|y| \le 0.4$ compared against preliminary CDF data. The dashed curve depicts the color-singlet contribution which includes direct $\Upsilon(1S)$ production as well as radiative feeddown from $\chi_{bJ}(1P)$ and $\chi_{bJ}(2P)$ states. The dot-dashed curve illustrates the color-octet contribution to $\Upsilon(1S)$ production. The solid curve equals the sum of the color-singlet and color-octet contributions and represents the total theoretical differential cross section. The $\Upsilon(1S)$ cross section predicted by the high energy gluon fragmentation approximation is shown by the dotted curve.

[3]The differential cross sections displayed in Fig. 6 and subsequent figures were calculated using the Martin-Roberts-Stirling set D0 (MRSD0) parton distribution functions evaluated at the renormalization scale $\mu = \sqrt{p_\perp^2 + M^2}$.

tion the dotted gluon fragmentation curve based upon the same value for $\mathcal{M}_8(\Upsilon(1S))$ at high $p_\perp$. The two cross sections diverge, however, at transverse momenta comparable to the $\Upsilon(1S)$ mass. This disparity demonstrates the breakdown of the fragmentation picture in the low energy regime.

The sum of the color-singlet and color-octet transverse momentum distributions is illustrated by the solid curve in Fig. 6. It represents the total theoretical $\Upsilon(1S)$ differential cross section. The solid curve's shape fits the data quite well except at the lowest point. At very small $p_\perp$, the color-singlet and color-octet cross sections are corrupted by collinear divergences as discussed in Sec. II. Since the intrinsic motion of incident partons inside colliding hadrons renders the differential cross section uncertain for $p_\perp \lesssim 2$ GeV, we have not attempted to remove the divergences from the dashed and dot-dashed curves. Instead, we simply regard the portion of the plot which runs below $p_\perp = 2$ GeV as untrustworthy. Above this low momentum cutoff, the predicted $\Upsilon(1S)$ distribution matches the data.

Analogous theoretical and experimental differential cross sections for $\Upsilon(2S)$ production in the rapidity region $|y| \leq 0.4$ are displayed in Fig. 7. The dashed color-singlet curve in the figure incorporates direct $\Upsilon(2S)$ production and radiative feeddown from $\chi_{bJ}(2P)$. The dot-dashed color-octet and dotted gluon fragmentation curves correspond to the squared matrix element $\mathcal{M}_8(\Upsilon(2S)) = (2.25 \pm 0.38) \times 10^{-3}$ GeV$^2$. The solid curve again illustrates the combined color-singlet and color-octet contributions to the $\Upsilon(2S)$ differential cross section. It clearly agrees with the CDF measurements much better than the color-singlet distribution alone.

We consider next the $\Upsilon(3S)$ differential cross section for which data is limited but interesting. The extent to which radiative $\chi_{bJ}(3P) \to \Upsilon(3S)\gamma$ transitions mediate $\Upsilon(3S)$ formation is unknown, for the $n = 3$ $P$-wave

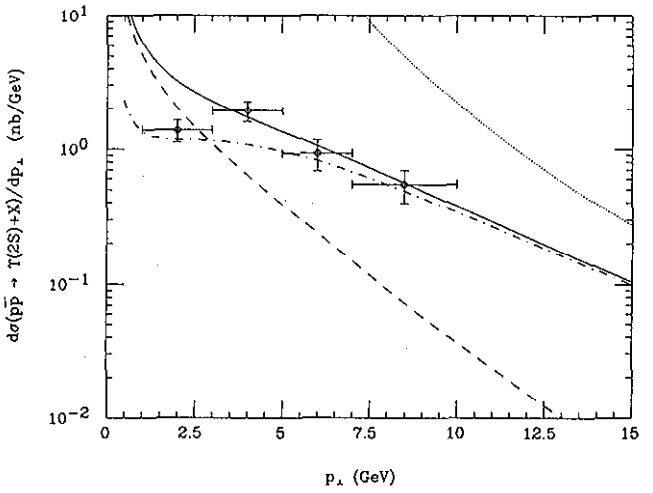


FIG. 7. Theoretical transverse momentum differential cross section for $\Upsilon(2S)$ production at the Tevatron in the rapidity interval $|y| \leq 0.4$ compared against preliminary CDF data. The curves in this figure are labeled the same as those in Fig. 6. The dashed color-singlet cross section includes $\Upsilon(2S)$ production and radiative feeddown from $\chi_{bJ}(2P)$.

states have never been observed. Although the $\Upsilon(4S)$ can electromagnetically decay to them, it lies above the $B\bar{B}$ threshold. As a result, $B(\Upsilon(4S) \to \chi_{bJ}(3P)\gamma)$ is very small,[4] and the $n = 3$ $P$-wave wave levels are rarely populated at $e^+e^-$ colliders. But at the Tevatron, $\chi_{bJ}(3P)$ bottomonia are directly created in hadronic reactions. Since the integrated $\Upsilon(3S)$ cross section measured by CDF is 10 times larger than the color-singlet model's prediction when only $\Upsilon(3S)$ production is taken into account, it is believed that $n = 3$ $P$-wave levels reside below the $B\bar{B}$ threshold and decay at a significant rate to the $n = 3$ $S$-wave state [10,15]. We consequently include their contributions into the dashed color-singlet curve in Fig. 8 using the measured $n = 2$ branching ratios $B(\chi_{bJ}(2P) \to \Upsilon(2S)\gamma)$ as estimates for their unknown $n = 3$ counterparts. The dot-dashed, dotted, and solid curves in the figure represent the color-octet, gluon fragmentation, and total differential cross sections based upon $\mathcal{M}_8(\Upsilon(3S)) = (0.53 \pm 0.24) \times 10^{-3}$ GeV$^2$. Given all the uncertainties, we can only say that agreement between the few measured $\Upsilon(3S)$ data points and the theoretical prediction appears adequate.

We now turn to the charmonium sector and examine prompt $J/\psi$ production at the Tevatron within the pseudorapidity interval $|\eta| \leq 0.6$. The $J/\psi$ cross section multiplied by the muon branching fraction $B(J/\psi \to \mu^+\mu^-) = 0.0597$ is illustrated in Fig. 9. The dashed curve in the figure depicts the color-singlet differential cross section that includes direct $J/\psi$ production

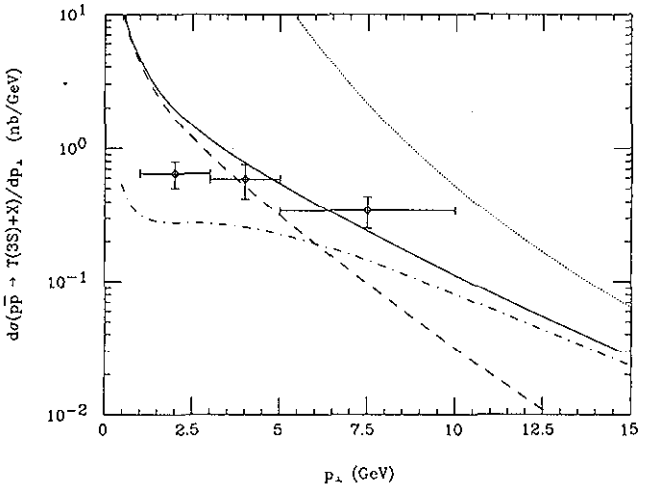


FIG. 8. Theoretical transverse momentum differential cross section for $\Upsilon(3S)$ production at the Tevatron in the rapidity interval $|y| \leq 0.4$ compared against preliminary CDF data. The curves in this figures are labeled the same as those in Fig. 6. The dashed color-singlet cross section includes $\Upsilon(3S)$ production and radiative feeddown from $\chi_{bJ}(3P)$. The measured $n = 2$ radiative branching ratios $B(\chi_{bJ}(2P) \to \Upsilon(2S) + \gamma)$ have been used as estimates for their unknown $n = 3$ counterparts $B(\chi_{bJ}(3P) \to \Upsilon(3S) + \gamma)$.

[4]CLEO has recently set a 5% upper limit on non-$B\bar{B}$ decays of the $\Upsilon(4S)$ [32].

and radiative feeddown from $\chi_{cJ}(1P)$ states. In calculating this curve, we employed the Buchmüller-Tye charmonium wave function values at the origin tabulated in Ref. [29] and the associated charm quark mass $M_c = 1.48$ GeV. Additional color-singlet contributions to the $J/\psi$ cross section from $\psi'$ production are small. The dot-dashed curve in Fig. 9 shows the color-octet $J/\psi$ cross section for the squared matrix element value $\mathcal{M}_8(J/\psi) = (0.68 \pm 0.03) \times 10^{-3}$ GeV$^2$. It is almost identical to the solid curve which represents the sum of the color-singlet and color-octet differential distributions. Comparing the dot-dashed color-octet and dotted gluon fragmentation curves with the CDF data in Fig. 9, we see that the fragmentation approximation appears to fit the experimental measurements better at small transverse momenta. But we must stress that this low energy agreement is fortuitous. The fragmentation prediction looks better only in the region where it becomes unreliable.

We finally consider prompt $\psi'$ production at the Tevatron. The observed differential cross section is 50 times larger than recent theoretical predictions based upon $c \to \psi'$ and $g \to \psi'$ fragmentation calculations [6,7]. These two $O(v^3)$ fragmentation processes create color-singlet $c\bar{c}[^3S_1^{(1)}]$ pairs at short-distance scales and yield comparable $\psi'$ production rates. At higher order in the NRQCD velocity expansion but lower order in perturbative QCD, the color-octet mechanism also mediates $g \to \psi'$ fragmentation through an intermediate $c\bar{c}[^3S_1^{(8)}]$ pair. The additional color-octet contribution to the $\psi'$ cross section which was not previously taken into account can readily resolve the factor of 50 discrepancy between theory and data [13,14].

We plot in Fig. 10 the $\psi'$ differential cross section multiplied by the muon branching fraction $B(\psi' \to \mu^+\mu^-) = 0.0077$. A pseudorapidity cut $|\eta| \leq 0.6$ has been applied to the distributions shown in the figure. The dashed curve represents just direct $\psi'$ production, for no other charmonium level below the $D\bar{D}$ threshold can decay to the $n = 2$ state. This color-singlet prediction drastically underestimates the measured differential cross section. Inclusion of color-octet contributions with $\mathcal{M}_8(\psi') = (0.20 \pm 0.01) \times 10^{-3}$ GeV$^2$ brings the magnitude and shape of the theoretical distribution into agreement with the data points displayed in Fig. 10. The color-octet mechanism thus appears to solve the CDF $\psi'$ problem.

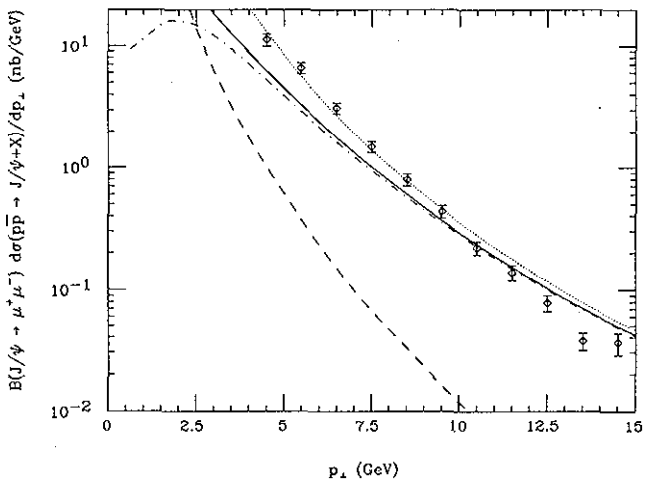


FIG. 9. Theoretical transverse momentum differential cross section for $J/\psi$ production at the Tevatron in the pseudorapidity interval $|\eta| \leq 0.6$ compared against preliminary CDF data. The dashed curve depicts the color-singlet contribution which includes direct $J/\psi$ production and radiative feeddown from $\chi_{cJ}$ states. The dot-dashed curve illustrates the color-octet contribution to $J/\psi$ production. The solid curve equals the sum of the color-singlet and color-octet contributions and represents the total theoretical differential cross section. The $J/\psi$ cross section predicted by the high energy gluon fragmentation approximation is shown by the dotted curve.

## IV. NRQCD MATRIX ELEMENTS

We have seen that heavy quarkonia production involves short and long distance physics. The high energy creation of color-singlet and color-octet $Q\bar{Q}$ pairs is perturbatively computable within the NRQCD effective theory. The subsequent low energy hadronization of these pairs into physical bound states is described in terms of nonrenormalizable operator matrix elements. NRQCD scaling rules determine the relative importance of different long-distance matrix elements and yield relations among them. We will use these rules to check he consistency of the fitted $\Upsilon$ and $\Psi$ amplitude values which we obtained in the preceding section.

We first recall the relations

$$\langle 0|\mathcal{O}_1^{\psi_Q}(^3S_1)|0\rangle = \frac{3N_c}{2\pi}|R(0)|^2 = O(M_Q^3 v_Q^3) \,, \tag{4.1}$$

$$\langle 0|\mathcal{O}_1^{\chi_{QJ}}(^3P_J)|0\rangle = \frac{3N_c}{2\pi}(2J+1)|R'(0)|^2 = O(M_Q^5 v_Q^5)$$

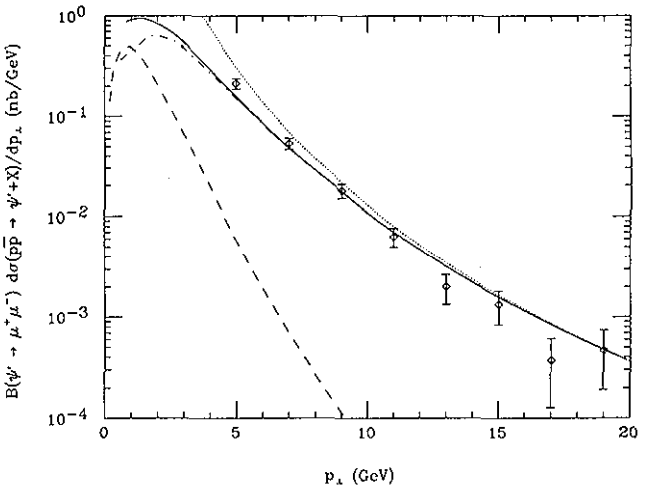


FIG. 10. Theoretical transverse momentum differential cross section for $\psi'$ production at the Tevatron in the pseudorapidity interval $|\eta| \leq 0.6$ compared against preliminary CDF data. The curves in this figures are labeled the same as those in Fig. 9. The dashed color-singlet cross section includes only direct $\psi'$ production.

between quarkonia radial wave functions at the origin and matrix elements of certain color-singlet four-quark operators in the NRQCD Lagrangian [16]. The details of these operators' definitions are discussed in Ref. [16], but they are not important to us. Instead, we are only interested in their scaling dependence upon the heavy quark mass $M_Q$ and velocity $v_Q$.

Using the Buchmüller-Tye wave function information tabulated in Ref. [29], we list the numerical values of color-singlet matrix elements that are relevant for $\Upsilon$ and $\Psi$ production in Table I. The entries in this table are consistent with the NRQCD power counting rules. In the $v_Q \to 0$ limit, the long-distance quarkonia matrix elements would be independent of the radial quantum number $n$. In actuality, the $n$ dependence of the $b\bar{b}$ sector entries is generally smaller than that of the $c\bar{c}$ values. This trend simply indicates that the NRQCD velocity expansion works better for bottomonia with $v_b^2 \simeq 0.08$ than for charmonia with $v_c^2 \simeq 0.23$.

NRQCD scaling rules can also be applied to color-octet four quark operators. We focus upon the matrix elements

$$\langle 0|\mathcal{O}_8^{\psi_Q}(^3S_1)|0\rangle = O(M_Q^3 v_Q^7) ,$$
$$\langle 0|\mathcal{O}_8^{\chi_{QJ}}(^3S_1)|0\rangle = O(M_Q^3 v_Q^5), \tag{4.2}$$

that determine the probability for $Q\bar{Q}[^3S_1^{(8)}]$ pairs to hadronize into $\psi_Q$ and $\chi_{QJ}$ quarkonia. These matrix elements appear in the decomposition of the total long-distance squared amplitude:

$$\mathcal{M}_8(\psi_Q(n)) = \frac{1}{24M_Q}\sum_{m\geq n}\Big\{\langle 0|\mathcal{O}_8^{\psi_Q(m)}(^3S_1)|0\rangle B(\psi_Q(m)\to\psi_Q(n)) + \sum_{J=0,1,2}\langle 0|\mathcal{O}_8^{\chi_{QJ}(m)}(^3S_1)|0\rangle B(\chi_{QJ}(m)\to\psi_Q(n)\gamma)+\cdots\Big\} \tag{4.3}$$

which reflects the different ways for a color-octet pair to materialize as a final $\psi_Q$. The infinite number of terms represented by the ellipsis contribute at higher order in the $v_Q$ or $\alpha_s$ expansions to color-octet $\psi_Q$ production than those explicitly displayed. So we will neglect them for simplicity.

We can extract numerical values for the NRQCD color-octet matrix elements in Eq. (4.2) by inserting our fitted values for $\mathcal{M}_8(\psi_Q)$ into Eq. (4.3). Combining $\mathcal{M}_8(J/\psi) = 6.8\times10^{-4}$ GeV$^2$ and $\mathcal{M}_8(\psi') = 2.0\times10^{-4}$ GeV$^2$ with the recent CDF finding that 32.3% of prompt $J/\psi$'s originate form $\chi_{cJ}$ decays [33], we deduce the charmonium color-octet matrix elements

$$\langle 0|\mathcal{O}_8^{J/\psi}(^3S_1)|0\rangle = 1.2\times10^{-2}\ \text{GeV}^3, \tag{4.4a}$$
$$\langle 0|\mathcal{O}_8^{\psi'}(^3S_1)|0\rangle = 7.3\times10^{-3}\ \text{GeV}^3, \tag{4.4b}$$
$$\langle 0|\mathcal{O}_8^{\chi_{c1}}(^3S_1)|0\rangle = 1.6\times10^{-2}\ \text{GeV}^3 . \tag{4.4c}$$

In the absence of additional bottomonium experimental information, we employ the NRQCD relation

$$\frac{\langle 0|\mathcal{O}_8^{\Upsilon(nS)}(^3S_1)|0\rangle}{\langle 0|\mathcal{O}_8^{\psi(nS)}(^3S_1)|0\rangle} \simeq \left(\frac{M_b}{M_c}\right)^3\left(\frac{v_b}{v_c}\right)^7 \tag{4.5}$$

to scale the $\Psi$ values in (4.4a) and (4.4b) to the $\Upsilon$ sector. We then obtain the color-octet matrix elements listed in Table II.

The numerical entries in this second table should be regarded as approximate estimates. Nonetheless, we see that the NRQCD scaling rules hold reasonably well for the color-octet matrix elements. The magnitudes of the entries in Table II appear consistent with each other and with those in Table I. These results thus provide a useful check on the entire color-octet quarkonia production picture.

## V. QUARKONIA SPIN ALIGNMENT

We have so far not considered final state spin information in our analysis. Previous investigations have found that quarkonia generated at large transverse momenta via gluon fragmentation processes such as $gg \to gg^* \to gg\chi_{QJ}$ are significantly polarized [11]. The source of this spin alignment can be traced to the fragmenting

TABLE I. Color-singlet matrix elements.

| Color-singlet matrix element | Numerical value | NRQCD scaling order |
|---|---|---|
| $\langle 0\|O_1^{J/\psi}(^3S_1)\|0\rangle$ | 1.2 GeV$^3$ | $M_c^3v_c^3$ |
| $\langle 0\|O_1^{\chi c1}(^3P_1)\|0\rangle$ | $3.2\times10^{-1}$ GeV$^5$ | $M_c^5v_c^5$ |
| $\langle 0\|O_1^{\psi'}(^3S_1)\|0\rangle$ | $7.6\times10^{-1}$ GeV$^3$ | $M_c^3v_c^3$ |
| $\langle 0\|O_1^{\Upsilon(1S)}(^3S_1)\|0\rangle$ | 9.3 GeV$^3$ | $M_b^3v_b^3$ |
| $\langle 0\|O_1^{\chi b1(1P)}(^3P_1)\|0\rangle$ | 6.1 GeV$^5$ | $M_b^5v_b^5$ |
| $\langle 0\|O_1^{\Upsilon(2S)}(^3S_1)\|0\rangle$ | 4.6 GeV$^3$ | $M_b^3v_b^3$ |
| $\langle 0\|O_1^{\chi b1(2P)}(^3P_1)\|0\rangle$ | 7.1 GeV$^5$ | $M_b^5v_b^5$ |
| $\langle 0\|O_1^{\Upsilon(3S)}(^3S_1)\|0\rangle$ | 3.5 GeV$^3$ | $M_b^3v_b^3$ |
| $\langle 0\|O_1^{\chi b1(3P)}(^3P_1)\|0\rangle$ | 7.7 GeV$^5$ | $M_b^5v_b^5$ |

TABLE II. Color-octet matrix elements.

| Color-octet matrix element | Numerical value | NRQCD scaling order |
|---|---|---|
| $\langle 0\|O_8^{J/\psi}(^3S_1)\|0\rangle$ | $1.2\times10^{-2}$ GeV$^3$ | $M_c^3v_c^7$ |
| $\langle 0\|O_8^{\chi c1}(^3S_1)\|0\rangle$ | $1.6\times10^{-2}$ GeV$^3$ | $M_c^3v_c^5$ |
| $\langle 0\|O_8^{\psi'}(^3S_1)\|0\rangle$ | $7.3\times10^{-3}$ GeV$^3$ | $M_c^3v_c^7$ |
| $\langle 0\|O_8^{\Upsilon(1S)}(^3S_1)\|0\rangle$ | $9.5\times10^{-3}$ GeV$^3$ | $M_b^3v_b^7$ |
| $\langle 0\|O_8^{\chi b1(1P)}(^3S_1)\|0\rangle$ | $4.3\times10^{-1}$ GeV$^3$ | $M_b^3v_b^5$ |
| $\langle 0\|O_8^{\Upsilon(2S)}(^3S_1)\|0\rangle$ | $5.7\times10^{-3}$ GeV$^3$ | $M_b^3v_b^7$ |
| $\langle 0\|O_8^{\chi b1(2P)}(^3S_1)\|0\rangle$ | $5.2\times10^{-1}$ GeV$^3$ | $M_b^3v_b^5$ |

gluon. At high energies, the virtual $g^*$ is off-shell only by $O(M^2/E^2)$ and is therefore nearly real and transverse. The $Q\bar{Q}[^3S_1^{(8)}]$ pair which the gluon forms at a short-distance scale must inherit its transverse alignment in order to conserve angular momentum. The subsequent long-distance evolution of the color-octet pair into a physical quarkonium state preserves the spins of the heavy quark and antiquark up to $O(\Lambda_{\rm QCD}/M)$ corrections. The final quarkonium's polarization state is then fixed by heavy quark spin symmetry [13].

It is interesting to examine the spin alignments of quarkonia produced via the color-octet mechanism at low energies as well. To do so, we decompose the short-distance part of the partonic squared amplitudes in Eq. (2.14) into separate longitudinal and transverse components:

$$\overline{\sum_{h=0}}|\mathcal{A}(q\bar{q}\to Q\bar{Q}^{(h)}[^3S_1^{(8)}]g)|^2=\frac{512\pi^3\alpha_s^3}{27M^2}\frac{4M^2\hat{s}}{(\hat{s}-M^2)^4}[4(\hat{t}^2+\hat{u}^2)-\hat{t}\hat{u}]\,, \tag{5.1a}$$

$$\overline{\sum_{|h|=1}}|\mathcal{A}(q\bar{q}\to Q\bar{Q}^{(h)}[^3S_1^{(8)}]g)|^2=\frac{512\pi^3\alpha_s^3}{27M^2}\frac{\hat{s}+M^4}{(\hat{s}-M^2)^4}\frac{\hat{t}^2+\hat{u}^2}{\hat{t}\hat{u}}[4(\hat{t}^2+\hat{u}^2)-\hat{t}\hat{u}]\,, \tag{5.1b}$$

$$\overline{\sum_{h=0}}|\mathcal{A}(gq\to Q\bar{Q}^{(h)}[^3S_1^{(8)}]q)|^2=-\frac{64\pi^3\alpha_s^3}{9M^2}\frac{2M^2\hat{t}}{[(\hat{s}-M^2)(\hat{t}-M^2)]^2}[4(\hat{s}^2+\hat{u}^2)-\hat{s}\hat{u}]\,, \tag{5.1c}$$

$$\overline{\sum_{|h|=1}}|\mathcal{A}(gq\to Q\bar{Q}^{(h)}[^3S_1^{(8)}]q)|^2=-\frac{64\pi^3\alpha_s^3}{9M^2}\frac{(\hat{s}^2+\hat{u}^2+2M^2\hat{t})(\hat{s}-M^2)^2-2M^2\hat{s}\hat{t}\hat{u}}{\hat{s}\hat{u}[(\hat{s}-M^2)(\hat{t}-M^2)]^2}[4(\hat{s}^2+\hat{u}^2)-\hat{s}\hat{u}]\,, \tag{5.1d}$$

$$\overline{\sum_{h=0}}|\mathcal{A}(gg\to Q\bar{Q}^{(h)}[^3S_1^{(8)}]g)|^2=-\frac{16\pi^3\alpha_s^3}{3M^2}\frac{2M^2\hat{s}}{(\hat{s}-M^2)^2}(\hat{t}^2+\hat{u}^2)\hat{t}\hat{u}\frac{27(\hat{s}\hat{t}+\hat{t}\hat{u}+\hat{u}\hat{s})-19M^4}{[(\hat{s}-M^2)(\hat{t}-M^2)(\hat{u}-M^2)]^2}\,, \tag{5.1e}$$

$$\overline{\sum_{|h|=1}}|\mathcal{A}(gg\to Q\bar{Q}^{(h)}[^3S_1^{(8)}]g)|^2=-\frac{16\pi^3\alpha_s^3}{3M^2}\frac{\hat{s}^2}{(\hat{s}-M^2)^2}\left[(\hat{s}-M^2)^4+\hat{t}^4+\hat{u}^4+2M^4\left(\frac{\hat{t}\hat{u}}{\hat{s}}\right)^2\right]$$
$$\times\frac{27(\hat{s}\hat{t}+\hat{t}\hat{u}+\hat{u}\hat{s})-19M^4}{[(\hat{s}-M^2)(\hat{t}-M^2)(\hat{u}-M^2)]^2}\,. \tag{5.1f}$$

The results in the $q\bar{q}\to Q\bar{Q}^{(h)}[^3S_1^{(8)}]g$ and $gq\to Q\bar{Q}^{(h)}[^3S_1^{(8)}]q$ channels were calculated using the covariant longitudinal and transverse spin sums discussed in Ref. [11]. The $gg\to Q\bar{Q}[^3S_1^{(8)}]g$ squared matrix elements were simply derived from our previously described helicity amplitude method. After summing over helicities in each mode and multiplying by $\mathcal{M}_8(\psi_Q)$, we reproduce the unpolarized expressions in Eq. (2.14).

The longitudinal squared amplitudes in (5.1a), (5.1c), and (5.1e) vanish as $\hat{s}/M^2\to\infty$, whereas their transverse counterparts in (5.1b), (5.1d), and (5.1f) approach constant limits. The gluon fragmentation prediction of total transverse alignment is therefore recovered at high energies. This asymptotic behavior can be seen in Fig. 11 where we plot the ratio

$$R_{\rm trans}=\frac{\sum_{|h|=1}\frac{d\sigma}{dp_\perp}(p\bar{p}\to Q\bar{Q}^{(h)}[^3S_1^{(8)}]X)}{\sum_h\frac{d\sigma}{dp_\perp}(p\bar{p}\to Q\bar{Q}^{(h)}[^3S_1^{(8)}]X)} \tag{5.2}$$

of transverse to total $b\bar{b}[^3S_1^{(8)}]$ and $c\bar{c}[^3S_1^{(8)}]$ differential cross sections as a function of $p_\perp$.[5] Figure 11 also demonstrates that color-octet pairs are strongly transverse even at low energies. This surprising phenomenon has a simple explanation. In the dominant $gg\to Q\bar{Q}^{(h)}[^3S_1^{(8)}]g$ channel, longitudinal color-octet pair production along the beam axis is prohibited by angular momentum conservation. The squared $h=0$ amplitude in (5.1e) therefore vanishes as $\hat{t}=-\frac{1}{2}(\hat{s}-M^2)(1-\cos\theta^*)$ or $\hat{u}=-\frac{1}{2}(\hat{s}-M^2)$

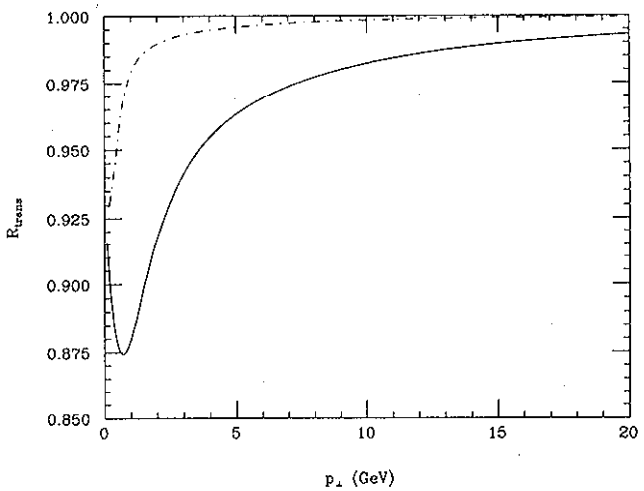


FIG. 11. Ratio $R_{\rm trans}$ of transversely aligned to total $Q\bar{Q}[^3S_1^{(8)}]$ differential cross sections plotted as a function of $p_\perp$. The solid and dot-dashed curves illustrate $R_{\rm trans}$ for $b\bar{b}[^3S_1^{(8)}]$ and $c\bar{c}[^3S_1^{(8)}]$ production, respectively.

[5]The shapes of the $b\bar{b}[^3S_1^{(8)}]$ and $c\bar{c}[^3S_1^{(8)}]$ curves in Fig. 11 are not exactly the same since their respective $|y|\le 0.4$ rapidity and $|\eta|\le 0.6$ pseudorapidity cuts are different.

$(1+\cos\theta^*)$ approaches zero, while its $|h|=1$ counterpart in (5.1f) remains finite. Since small angle scattering dominates this $2\to 2$ partonic process, most $Q\bar{Q}[^3S_1^{(8)}]$ pairs are formed at $|\cos\theta^*|\simeq 1$. As a result, they are transversely aligned independent of their energy. The ratios of the $h=0$ and $|h|=1$ squared amplitudes in the $q\bar{q}\to Q\bar{Q}^{(h)}[^3S_1^{(8)}]g$ and $gq\to Q\bar{Q}^{(h)}[^3S_1^{(8)}]q$ channels similarly vanish at $\hat{t}\to 0$ or $\hat{u}\to 0$.

The nearly 100% transverse alignment of $c\bar{c}[^2S_1^{(8)}]$ pairs should be directly observable in $\psi'$ production at the Tevatron if the color-octet mechanism resolves the $\psi'$ problem. Color-octet production then dominates over all other prompt $\psi'$ sources by a factor of 50. Heavy quark spin symmetry guarantees that $\psi'$ spin alignments equal those of their $c\bar{c}[^3S_1^{(8)}]$ progenitors in the $M_c\to\infty$ limit [13]. Finite charm mass effects somewhat degrade final $\psi'$ polarizations. But experimental observation of a large transverse $\psi'$ spin alignment would provide strong support for the color-octet production picture.

Other $S$ and $P$-wave charmonia and bottomonia can also inherit a sizable spin alignment. Their helicity level populations depend upon the color-octet matrix elements in Table II. Detailed predictions for quarkonium polarizations resulting from color-singlet and color-octet production will be presented elsewhere. But we emphasize here that experimental measurements of $\Upsilon$, $\Psi$ and $\chi$ spin alignments will provide valuable tests of our understanding of basic quarkonium physics.

## VI. CONCLUSION

In this paper, we have examined color-octet production of heavy quarkonia at hadron colliders. Color-octet diagrams arise at the same order in perturbative QCD as their color-singlet analogues and reduce to the dominant set of gluon fragmentation graphs in the high energy limit. They must therefore be included in bottomonia and charmonia production computations. As we have seen, color-octet contributions to $\Upsilon$ and $\Psi$ differential cross sections eliminate large disparities between earlier predictions and recent measurements. The long-distance matrix element values needed to bring theory into line with experiment are consistent with NRQCD scaling rules. We have also found that the color-octet mechanism yields $Q\bar{Q}[^3S_1^{(8)}]$ pairs which are nearly 100% transversely aligned at all $p_\perp$. Observation of large quarkonia spin alignments would provide strong support for the color-octet production picture.

A number of extensions of this work would be interesting to pursue. For example, a low transverse momentum study should reveal that quarkonia distributions vanish rather than diverge as $p_\perp\to 0$. In order to compute the cross section turnover, it will be necessary to factorize collinear singularities in both the color-singlet and color-octet channels into incident parton distribution functions and resum soft gluon effects. Collinear divergence factorization also needs to be performed before differential quarkonia distributions can be integrated. We expect color-octet contributions to significantly enhance existing predictions for total $\Upsilon$ and $\Psi$ production rates. Comparison of integrated quarkonium cross sections with fixed target measurements will provide an important means for testing the long-distance matrix element values which we have found using collider data. Finally, all the results in this article can be applied to the study of quarkonia production at the next generation of hadron colliders. We look forward to further surprises in quarkonium physics coming from machines such as the CERN Large Hadron Collider (LHC) well into the next century.

## ACKNOWLEDGMENTS

We have benefited from helpful discussions with many colleagues and friends. We wish to especially thank Eric Braaten, Michelangelo Mangano, Mikolaj Misiak, Ivan Muzinich, Vaia Papadimitriou, David Politzer, Chris Quigg, Elizabeth Simmons, Sandip Trivedi, and Mark Wise for sharing their insight with us. The work of P.C. was supported in part by the DuBridge Foundation and by the U.S. Dept. of Energy under DOE Grant No. DE-FG03-92-ER40701. The work of A.K.L. was supported in part by the U.S. Dept. of Energy under DOE Grant No. DE-FG03-92-ER40701.

[1] E. Braaten and T. C. Yuan, Phys. Rev. Lett. **71**, 1673 (1993).
[2] E. Braaten, K. Cheung, and T. C. Yuan, Phys. Rev. D **48**, 4230 (1993).
[3] Y.-Q. Chen, Phys. Rev. D **48**, 5181 (1993).
[4] E. Braaten and T. C. Yuan, Phys. Rev. D **50**, 3176 (1994).
[5] T. C. Yuan, Phys. Rev. D **50**, 5664 (1994).
[6] E. Braaten, M. A. Doncheski, S. Fleming, and M. L. Mangano, Phys. Lett. B **333**, 548 (1994).
[7] D. P. Roy and K. Sridhar, Phys. Lett. B **339**, 141 (1994).
[8] M. Cacciari and M. Greco, Phys. Rev. Lett. **73**, 1586 (1994).
[9] CDF Collaboration, F. Abe *et al.*, Fermilab-Conf-94/136-E (1994) (unpublished).
[10] CDF Collaboration, F. Abe *et al.*, Fermilab-Conf-95/128-E (1995) (unpublished).
[11] P. Cho, S. Trivedi, and M. Wise, Phys. Rev. D **51**, 2039 (1995).
[12] F. E. Close, Phys. Lett. B **342**, 369 (1995).
[13] P. Cho and M. Wise, Phys. Lett. B **346** 129 (1995).
[14] E. Braaten and S. Fleming, Phys. Rev. Lett. **74**, 3327 (1995).
[15] CDF Collaboration, F. Abe *et al.*, Fermilab-Conf-94/221-E (1994) (unpublished).
[16] G. T. Bodwin, E. Braaten, and G. P. Lepage, Phys. Rev. D **51**, 1125 (1995).
[17] W. E. Caswell and G. P. Lepage, Phys. Lett. **167B**, 437 (1986).
[18] G. P. Lepage, L. Magnea, C. Nakhleh, U. Magnea, and K. Hornbostel, Phys. Rev. D **46**, 4052 (1992).
[19] For reviews of quarkonia potential model calculations,

see *Quarkonia*, edited by W. Buchmüller (North-Holland, Amsterdam, 1992).
[20] R. Baier and R. Rückl, Z. Phys. C. **19**, 251 (1983).
[21] R. Gastmans, W. Troost, and T. T. Wu, Nucl. Phys. **B291**, 731 (1987).
[22] B. Humpert, Phys. Lett. B **184**, 105 (1987).
[23] G. A. Schuler, CERN-TH.7170/94 (1994) (unpublished) and references therein.
[24] J. H. Kühn, J. Kaplan, and E. G. O. Safiani, Nucl. Phys. **B157**, 125 (1979).
[25] B. Guberina, J. H. Kühn, R. D. Peccei, and R. Rückl, Nucl. Phys. **B174**, 317 (1980).
[26] T. D. Lee, *Particle Physics and Introduction to Field Theory* (Harwood Academic, Chur, Switzerland, 1988).
[27] P. Cho and A. K. Leibovich, Report No CALT-68-2026, 1995 (unpublished).
[28] R. Mertig, M. Böhm, and A. Denner, Comput. Phys. Commun. **64**, 345 (1991).
[29] E. J. Eichten and C. Quigg, Phys. Rev. D **52**, 1726 (1995).
[30] M. Cacciari, M. Greco, M. L. Mangano, and A. Petrelli, Phys. Lett. B **356**, 553 (1995).
[31] W. Buchmüller and S.-H. H. Tye, Phys. Rev. D **24**, 132 (1981).
[32] CLEO Collaboration, CLEO CONF 94-6 (1994) (unpublished).
[33] CDF Collaboration, G. Bauer, talk presented at the $p\bar{p}$ 95 Workshop, 1995 (unpublished).